The Gothic Shale at Greater Aneth Oil Field, Paradox Basin, Southeastern Utah: Seal for Hydrocarbons and Carbon Dioxide Geologic Sequestration

Thomas C. Chidsey, Jr. and Stephanie Carney,
Utah Geological Survey,
Salt Lake City, Utah

Jason Heath,
New Mexico Institute of Mining and Technology,
Socorro, New Mexico

Thomas Dewers,
Sandia National Laboratories,
Albuquerque, New Mexico

Abstract

Greater Aneth oil field, Utah's largest oil producer, was discovered in 1956 and has produced over 451 million barrels (bbls) of oil. Located in the Paradox Basin of southeastern Utah, Greater Aneth is a stratigraphic trap producing from the Pennsylvanian Paradox Formation. Because it represents an archetype oil field of the western U.S., Greater Aneth was selected to demonstrate combined enhanced oil recovery (EOR) and carbon dioxide (CO_2) sequestration. The Aneth Unit in the northwestern part of the field has produced 149 million bbls of the estimated 450 million bbls of OOIP—a 33% recovery rate. The large amount of remaining oil made the Aneth Unit ideal to demonstrate both CO_2 storage capacity and EOR by CO_2 flooding.

Within the Paradox Formation, the Gothic shale seals the underlying Desert Creek reservoir zone. The Gothic shale ranges in thickness from 5 to 27 ft, averaging 15 ft. Within the Aneth Unit, it is remarkably uniform consisting of black to gray, laminated to thin-bedded, dolomitic marine shale. The Gothic contains total organic carbon as high as 15% with type III and mixed type II-III kerogen. Natural fractures include horizontal and inclined (30 to 44°) with evidence of shear in the form of slickensides; some mineralization is present. Geomechanical, petrophysical, petrological, and geochemical analyses were conducted to determine (1) the geologic controls on sealing effeciency (using x-ray diffraction [XRD], scanning electron microscopy [SEM], and thin sections to interpret mercury injection capillary pressure data), (2) effects of pressure changes on seal efficiency due to CO_2 injection and storage, and (3) chemical interaction between CO_2 and the seal at its contact with the reservoir through time.

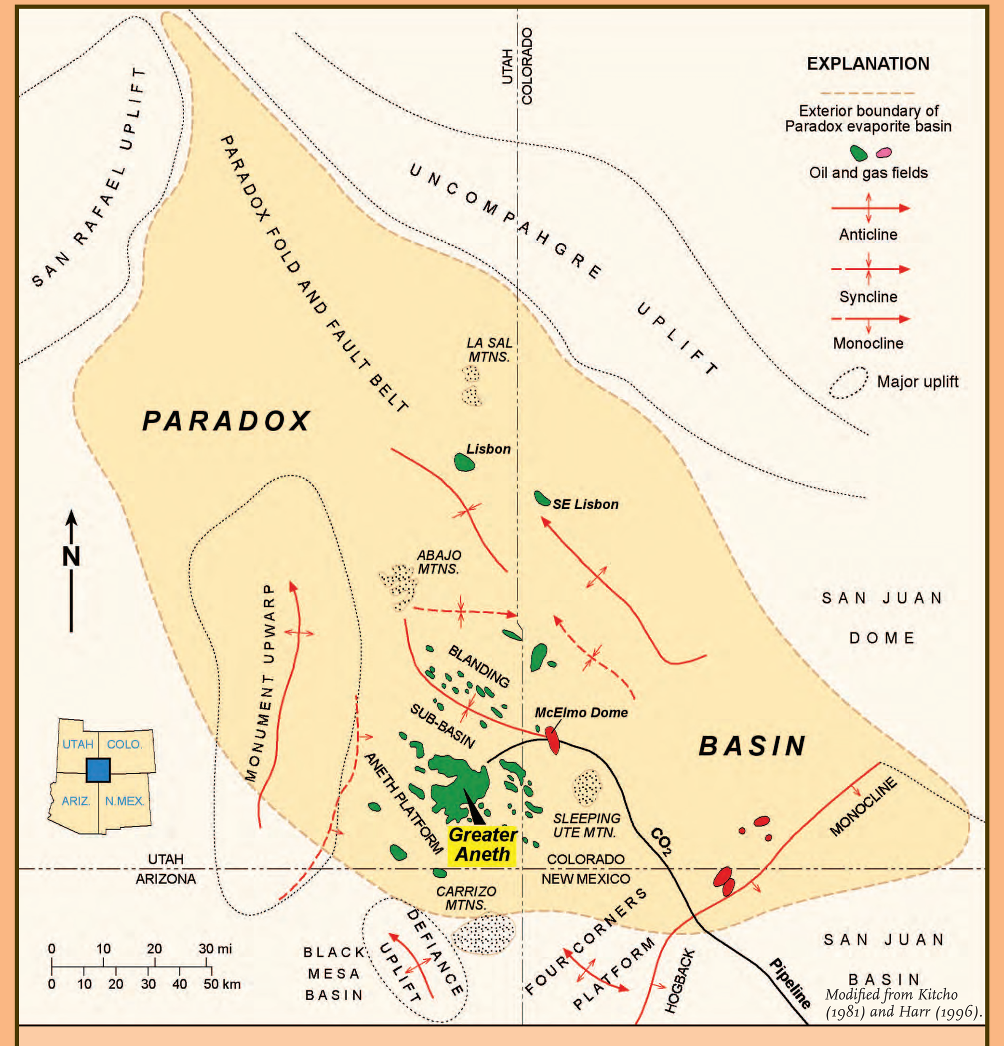

Location map of the Paradox Basin and major oil and gas fields.

Acknowledgments

This ongoing research is performed under the direction of the New Mexico Institute of Mining and Technology, Brian McPherson, Project Manager and Principal Investigator, as part of the Southwest Regional Partnership on Carbon Sequestration—Phase II: Field Demonstrations Project. This project is funded by the U.S. Department of Energy through the National Energy Technology Laboratory, Contract No. DE-FC26-05NT42591. Support is also being provided by the Utah Geological Survey (UGS), New Mexico Institute of Mining and Technology, and Sandia National Laboratories. Sandia is a multiprogram laboratory operated by Sandia Corporation, a Lockheed Martin Company, for the U.S. Department of Energy under contract DE-ACOC4-94AL85000.

Geochemical, petrophysical, petrographic, and geomechanical analyses were conducted by TerraTek, Salt Lake City, Utah; Sandia National Laboratories, Albuquerque, New Meixco; and Poro-Technology, Houston, Texas. We thank Wagner Petrographic in Lindon, Utah, for preparing fluorescent red-dye epoxied thin sections and billets for examination of natural fractures and organics by the laser scanning confocal microscope. The poster design was by Stevie Emerson of the UGS. Figures were prepared by James Parker and Cheryl Gustin of the UGS, TerraTek, and Sandia National Laboratories; core description was provided by S. Robert Bereskin, Bereskin & Associates, Inc., Michael Laine, Ammon McDonald, Thomas Dempster, and Brad Wolverton of the UGS assisted with sample preparation and core photography.

General Field Overview

Discovery Well

- Texaco #1 Navajo C
- Total depth – 5923 ft
- Completed February 6, 1956
- IPF – 568 bbls of oil per day
- Initial pressure – 2170 pounds per square inch of area
- Gas-oil ratio – 3448:1

Reservoir Data

- Productive area – 48,260 acres
- Net pay – 50 ft
- Porosity – 10.2%
- Permeability – 10 millidarcies (mD), range 3-30 mD
- Water saturation – 24%
- Bottom-hole temperature – 125°F
- Type of drive – fluid expansion and solution gas
- Lithology – limestone (algal boundstone and oolitic-, peloidal-, and skeletal grainstone/ packstone), as well as finely crystalline dolomitic limestone

Production Data (as of January 1, 2009) and Reserves

- Cumulative oil – 451,033,186 bbls
- Cumulative gas – 396 billion cubic feet (BCF)
- Cumulative water – 1,526,708,595 bbls
- Active wells – 456
- In-place total oil reserves – 1100 million bbls
- Type of secondary recovery – waterflood and CO_2 flood, horizontal drilling

Location of Greater Aneth and surrounding oil fields, Paradox Basin.

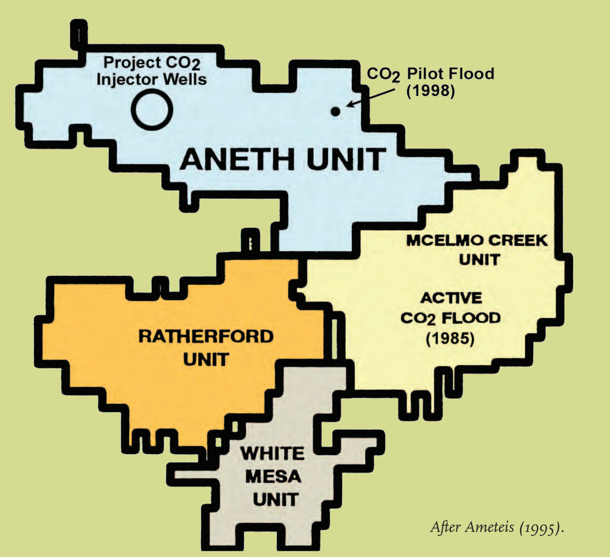

Units within Greater Aneth field.

Oil Characteristics

- Type – paraffinic
- Color – dark green
- API gravity – 40-42°
- Viscosity, SUS – 0.53-0.54 centipoise (cp)
- Pour point – 10°F (-12°C)
- Sulfur, wt% – 0.20%
- Nitrogen – 0.04%

Aneth Unit

- 16,320 acres
- 421 million bbls of oil in place
- Over 149 million bbls recovered (33% recovery)
- Waterflood, 1962
- Infill drilling to 40 acres, 1982; infilling to 20 acres, 1988
- Horizontal drilling program, 1994
- CO_2 flood, 2007; 28 BCF injected as of March 2009

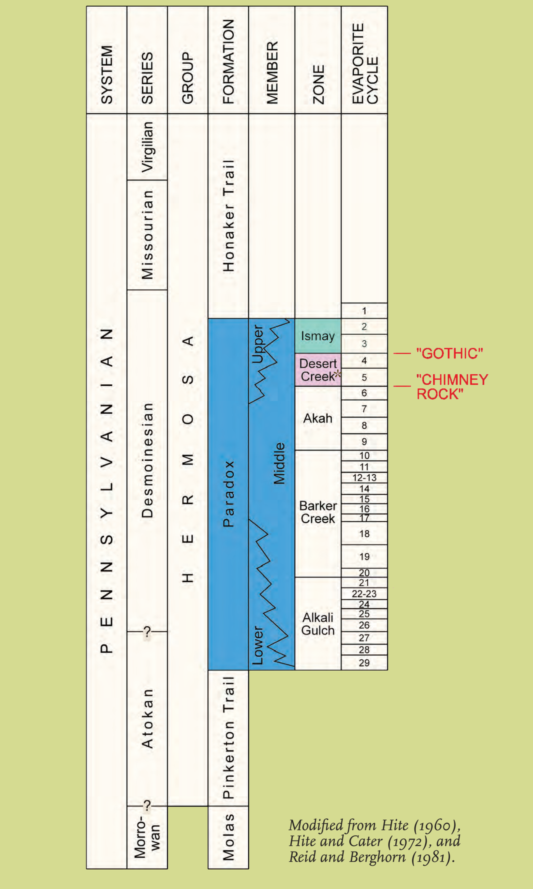

Pennsylvanian stratigraphy of the Paradox Basin.
*Reservoir Unit at Greater Aneth field.

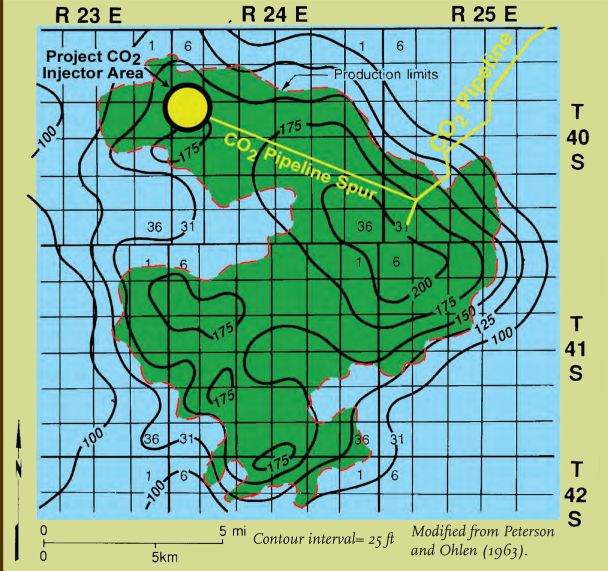

Generalized thickness map: Desert Creek zone.

Gothic Shale Seal

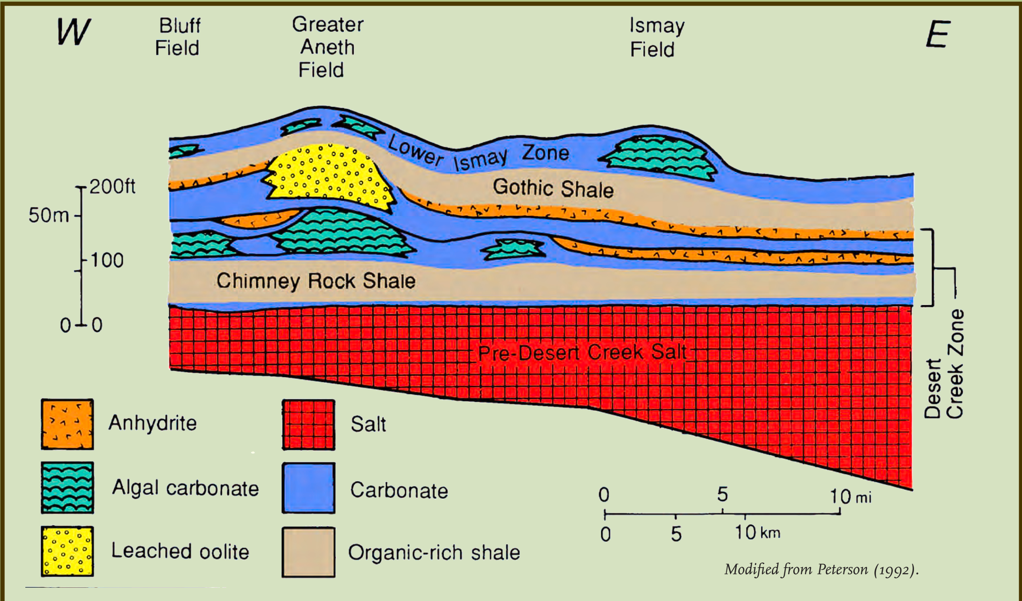

Diagrammatic lithofacies cross section.

Gothic shale in the Pennsylvanian Paradox Formation exposed along the Honaker Trail, San Juan River Canyon, Utah.

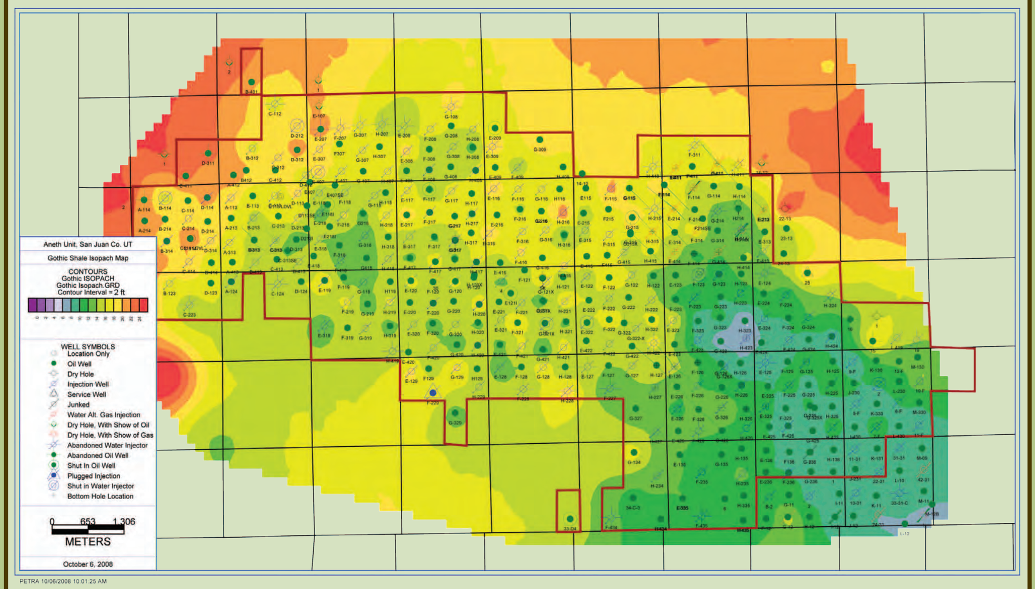
Thickness of the Gothic shale, Aneth Unit.

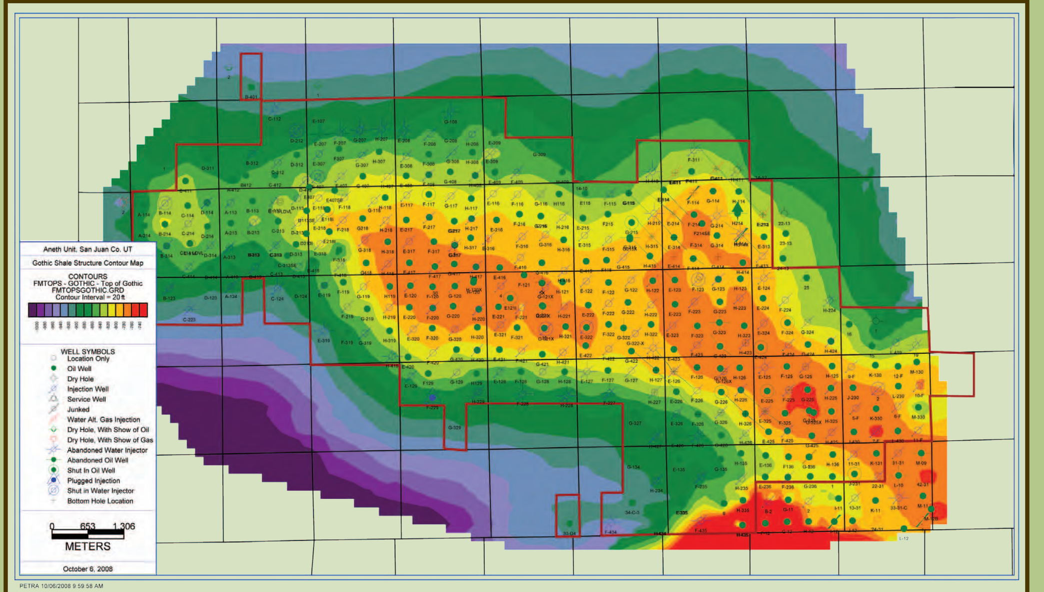
Structure on the top of the Gothic shale, Aneth Unit.

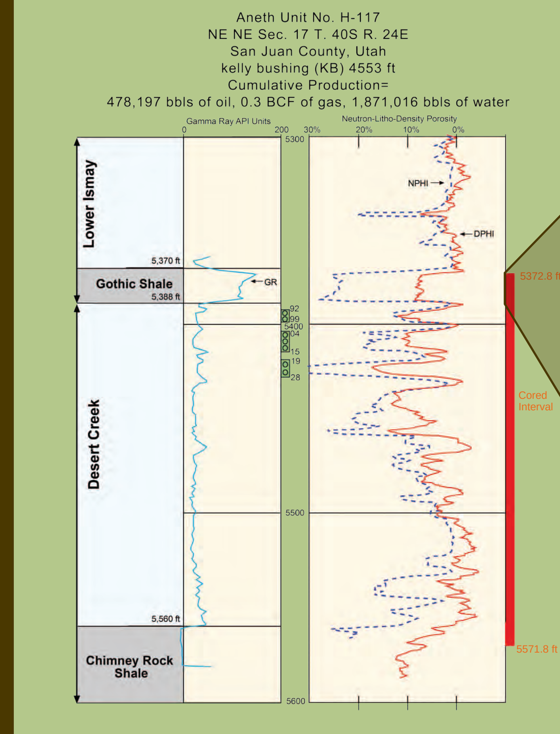

Interpreted geophysical well log, Aneth Unit H-117 well.

Gothic shale core (unslabbed), Aneth Unit H-117 well.

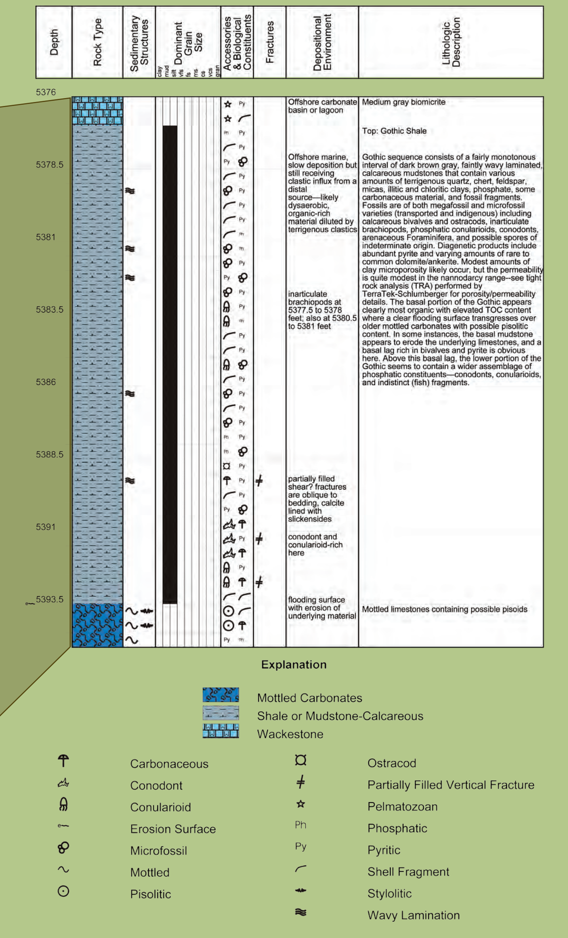
Gothic shale core description.

GEOCHEMISTRY

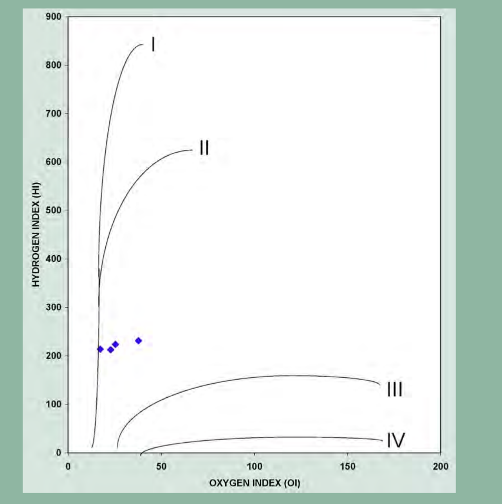

Kerogen type determination from TOC and Rock-Eval pyrolysis data. Types I and II will generate oil; type III, gas; and type IV, little or no hydrocarbon.

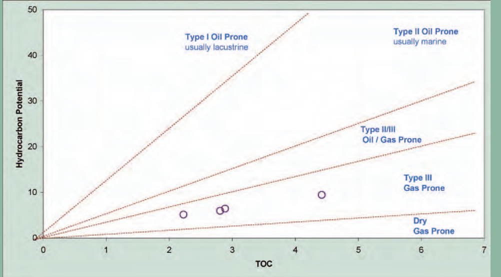

Kerogen quality.

Basic Geochemical Measurements from the Aneth Unit H-117 Well

Depth	As-Received Bulk Density	TOC	S_1	S_2	S_3	Tmax	HI	OI	S_1/TOC	PI	Calc Ro
ft	g/cc	Wt. %	mg/g	mg/g	mg/g						
5379.40	2.570	2.89	2.09	6.45	0.73	445	224	25	72	0.24	0.85
5382.80	2.561	2.81	2.16	5.97	0.64	451	213	23	77	0.27	0.96
5386.90	2.572	2.23	1.93	5.15	0.84	444	231	38	87	0.27	0.83
5390.80	2.522	4.42	2.39	9.46	0.76	449	214	17	54	0.20	0.92

S_1 is the amount of free hydrocarbons (gas and oil) in the sample (in milligrams of hydrocarbon per gram of rock). If S_1 >1 mg/g, it may be indicative of an oil show.
S_2 is the amount of hydrocarbons generated through thermal cracking of nonvolatile organic matter. S_2 is an indication of the quantity of hydrocarbons that the rock has the potential of producing should burial and maturation continue.
S_3 is the amount of CO_2 (in milligrams CO_2 per gram of rock) produced during pyrolysis of kerogen. S_3 is an indication of the amount of oxygen in the kerogen.
Tmax is the temperature at which the maximum release of hydrocarbons from cracking of kerogen occurs during pyrolysis (top of S_2 peak). Tmax is an indication of the stage of maturation of the organic matter.
HI is the hydrogen index (HI = [100 x S_2]/TOC).
OI is the oxygen index (OI = [100 x S_3]/TOC).
PI is the production index (PI = S_1/[S_1 + S_2]).

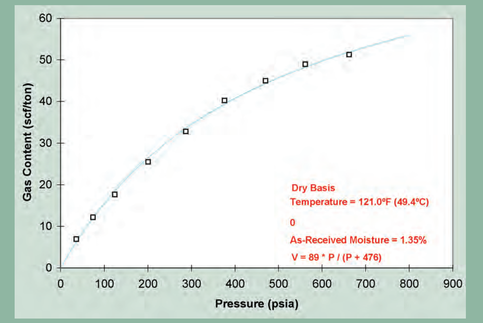

Methane adsorption isotherm, 5390.8 ft.

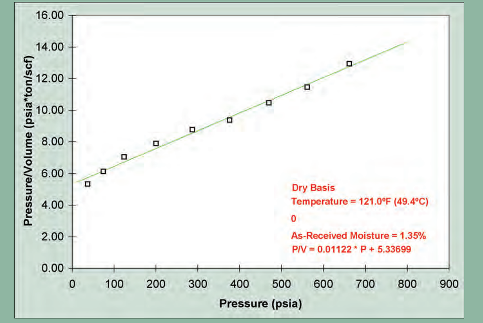

Adsorption Langmuir plot, 5390.8 ft.

Methane Adsorption Isotherm, 5390.8 ft

Dry Basis		TOC = 4.42%	
Sample Weight = 224.61 g		As-Received Moisture = 1.35%	
Particle Size = < 12 Mesh			
Temperature = 121.0°F (49.4°C)			
Methane Adsorption			
Pressure		Gas Content (Dry Basis)	
(psia)	(MPa)	(scf/ton)	(scc/g)
37	0.26	6.9	0.22
75	0.52	12.1	0.38
124	0.85	17.7	0.55
201	1.39	25.5	0.80
287	1.98	32.8	1.02
376	2.59	40.2	1.25
471	3.25	45.0	1.40
561	3.87	49.0	1.53
662	4.56	51.2	1.60
Langmuir Coefficients $V_L = 89.1 * P_L / (P_L + 475.7)$			
P_L		V_L (Dry Basis)	
(psia)	(MPa)	(scf/ton)	(scc/g)
475.7	3.28	89.1	2.8

X-Ray Fluorescence

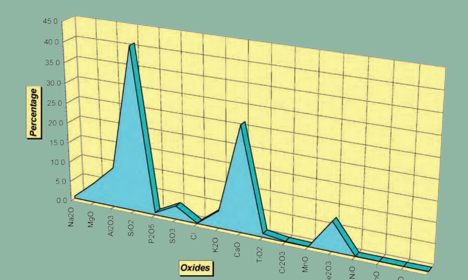

X-ray fluorescence data for selected 2 foot intervals over the length of the core. The graph shows 41% silicon dioxide, 26% calcium oxide, 10% aluminum oxide, 7% iron oxide, 5% magnesium oxide, 4% potassium oxide, and 3% sulfur trioxide plus various small amounts of trace oxides.

X-Ray Diffraction

Results from bulk and oriented (clay fraction dominant) samples. All data is referenced to the magnitude of the quartz peak. Offsets are imposed on the data for the purpose of comparison.

Bulk Analysis

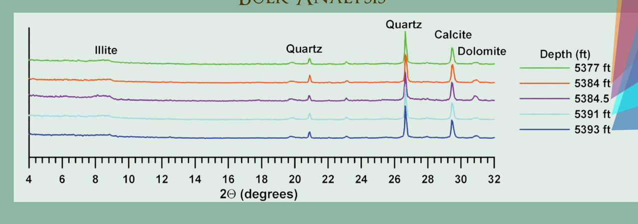

The bulk analysis (powder) figure shows the consistency of mineralogical composition over the range of the core. The indistinct illite peak is consistent as are the strong quartz, calcite, and dolomite peaks.

Oriented Sample Analysis (Sedimented)

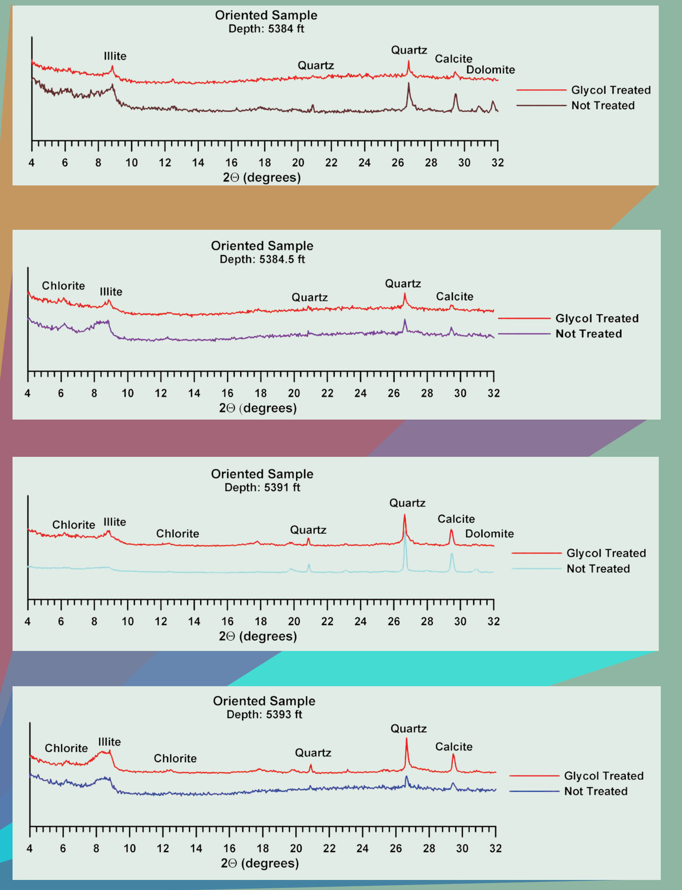

The individual sample figures illustrate the difference in results between the glycol treated samples and non-treated samples. XRD analysis of the glycol treated samples in some cases resulted in a definite illite peak while in other cases enhanced the existing illite peak. In both cases the presence of a small percentage of expandable clays (approx. 10%) such as smectite is inferred.

PETROGRAPHY

5379.4 FT

Argillaceous shale lithotype in Gothic shale shown at low magnification. Clay matrix supports a few elongate chert stringers likely representing microfossils, scattered pyrite (black) and silt (white), as well as silt-sized calcite crystals (stained red, dual carbonate stain). The magenta lines at the bottom of the image are induced stress-release fractures.

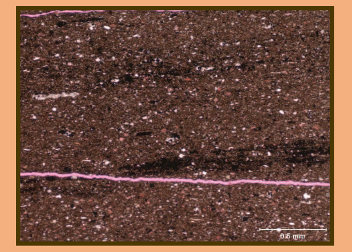

Same as image to the left at slightly higher magnification. Black streaks are pyrite concentrated parallel to bedding.

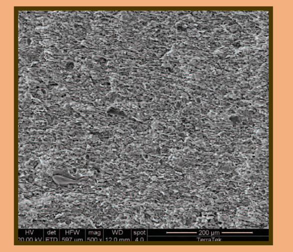

SEM overview of texture in uniform, non-laminated argillaceous shale. A few siliceous and calcareous fragments float in a matrix of crenulated clays.

Methods: Core pieces were impregnated with a low-viscosity red-dye fluorescent epoxy resin under vacuum. The epoxied samples were mounted to standard thin section slides. Thin sections were dual stained for identification of carbonate minerals using a mixture of potassium ferricyanide and Alizarin Red S. Photomicrographs were taken using a petrographic micrograph with plane polarized light, cross polarized light, and reflected UV light with rhodamine filter. Electron petrography included scanning electron microscopy (SEM) and backscattered electron (BSE) imaging with energy dispersive X-ray spectroscopy (EDS).

Methods: Microstructures and distribution of organic material in non-epoxied samples were imaged using a Zeiss 510-Meta Laser Scanning Confocal Microscope (LSCM). Green, yellow-orange, and red-fluorescing material was imaged at 63x and 100x using simultaneous excitation at 488 nm via an argon laser, 543 nm via a HeNe laser, and 633 nm via a second HeNe laser. Emission spectra was measured at wavelengths between 499-531 nm (green), 563-617 nm (yellow-orange), and 649-798.9 (red). 3D images were obtained using a 63x/1.4NA oil DIC Plan Apochromat lense (with voxel size of 0.28 or 0.14 microns in x and y and 1.1. or 0.75 microns in z) and a 100x/1.45NA Alpha Plan-Fluar lense (with voxel size of 0.088 microns in x and y and 0.5 microns in z) using non-fluorescing oil (no fluorescent dyes were applied to the sample).

5380 FT

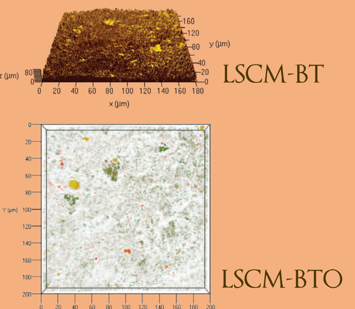

Corresponding LSCM images of a bedding surface: the upper image shows topography in an oblique view, and the lower shows green, yellow-orange, and red fluorescing material. Red material is typically spherical and probably co-located with pyrite framboids. Green fluorescing material is the most abundant organic material, reflective of a primary depositional process that distributed the organic material.

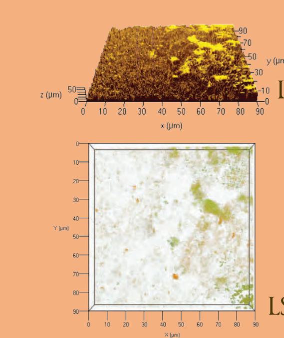

Corresponding LSCM images of surface broken perpendicular to bedding: the upper image shows topography in an oblique view, and the lower shows a relatively high resolution image of green, yellow-orange, and red fluorescing material.

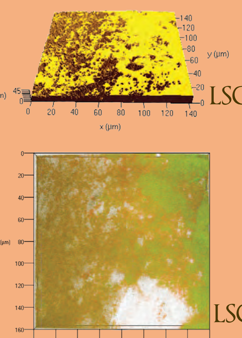

Corresponding LSCM images of surface broken perpendicular to bedding: the upper image show topography in an oblique view, and the lower shows green, yellow-orange, and red fluorescing material.

BSE IMAGES 5378.1 FT

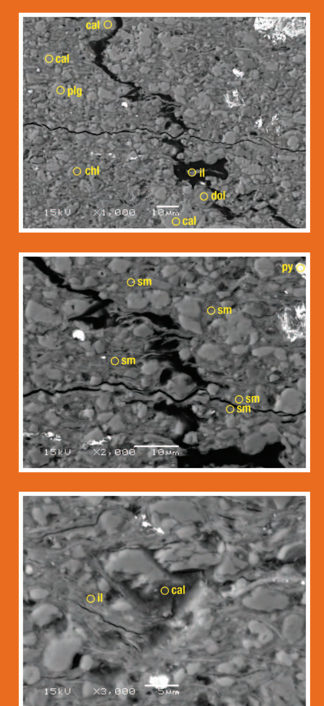

py = pyrite
dol = dolomite
cal = calcite
sm = smectite
il = illite
chl = chlorite
plg = plagioclase

Argillaceous mudstone. Weak lamination is defined by micas and compacted cherty microfossils (white, lower right). Pink specks in the matrix are stained, silt-sized calcite particles. The argillaceous matrix also supports dispersed medium silt grains.

The grain at center is a compacted cherty microfossil in argillaceous mudstone matrix. Such forms are characteristic throughout this interval of Gothic shale, and commonly indicate microcrystalline quartz as a matrix cement.

Reflected UV light with rhodamine filter of the image above showing swarms of orange pinpoints that indicate intercrystalline micropores. Brighter fluorescence inside the microfossil is attributed to mineral fluorescence.

5382.8 FT

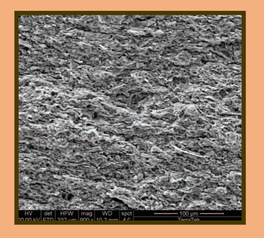

SEM overview of argillaceous mudstone highlighting distinct grain orientation. Compacted packets of clays are the main textural feature, separated by planar parting surfaces. The clay-rich matrix hosts numerous micropores; authigenic pyrite is ubiquitous.

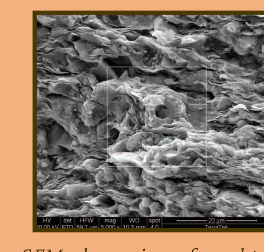

SEM closer view of mudstone matrix showing wavy parting planes between clay packets. The tube at center (box) is enlarged in the next image.

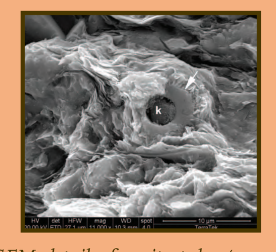

SEM detail of pyrite tube (arrow) shown in the previous image. The form represents a replaced microfossil, and is lined with scruffy kerogen residue (k). Note the flakey matrix clays, likely illite and/or mixed layer illite-smectite.

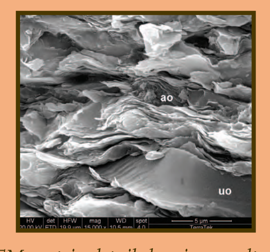

SEM matrix detail showing unaltered and altered carbonaceous material. The smooth particle at lower right (uo) represents a discrete carbonaceous grain with little alteration. At top center, a particle representing a different class of organics, embedded between clay flakes (ao), displays fuzzy, rough texture.

5386.9 FT

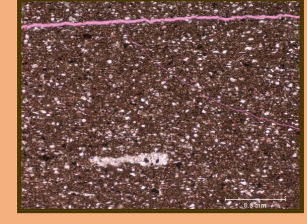

Silty calcareous/argillaceous mudstone with induced fracture at the top of the image (magenta). Finely disseminated carbonaceous material is visible in the matrix, as are abundant silt grains, calcite crystals (pink) and pyrite. Note cherty microfossil at bottom of image.

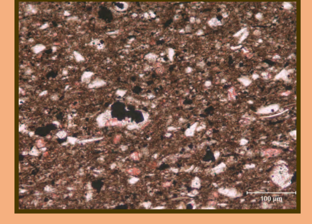

Matrix detail highlighting dominant textural components. Quartz silt, silt-sized calcite (red), mica flakes, and authigenic pyrite float in a predominantly clay matrix.

SEM showing calcareous argillaceous mudstone containing many calcite particles and quartz silt grains. Calcareous/argillaceous matrix supports a thin shell fragment in the lower part of the image, replaced by calcite and quartz. Cement-coated clay flakes appear to preserve a microporous structure.

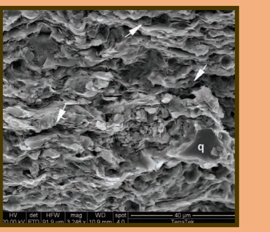

This medium magnification SEM view of the matrix shows elongate pores parallel to parting planes (arrows). The micropore network is also visible, consisting of voids with sizes from 2-10 microns, and flattened in shape. The irregular grain at right is quartz (q).

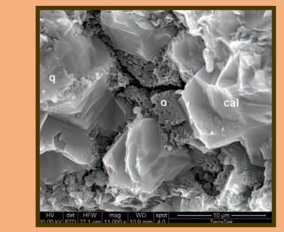

SEM detail of the replaced shell fragment in the previous image. The foamy porous material at center is organic (o). Blocky crystals at left are quartz (q); at right is a calcite crystal (cal).

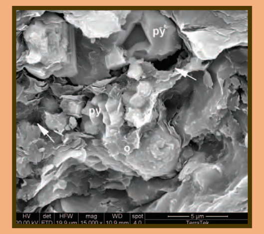

This SEM image illustrates a common association of pyrite with carbonaceous material. The perforated flakes of organics (o) surround pyrite crystals (py). Intercrystalline porosity (arrows) is believed to have developed through alteration of organics.

5390.8 FT

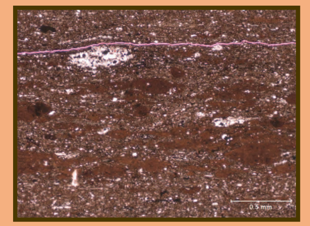

Overview of phosphatic argillaceous mudstone. This part of the image shows flattened, amalgamated pellets (lighter brown), which SEM show to be phosphatic in composition. The matrix overview highlights compacted siliceous forms (white) composed of chert, and flattened fecal pellets in a mixed siliceous/argillaceous matrix. The lighter brown matrix color and abundance of siliceous fossils, as well as phosphatic pellets suggest a siliceous matrix cement component.

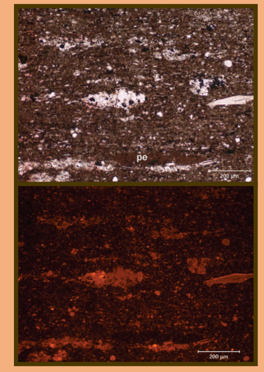

Closer view showing microfossils, micas, a fecal pellet (pe) and a conodont supported by argillaceous matrix. Unstained portion of the slide.

Same area shown in the image above except under reflected UV light. Note the matrix micropores appearing as bright orange dots. Dull orange is mineral fluorescence. (Reflected UV light with rhodamine filter).

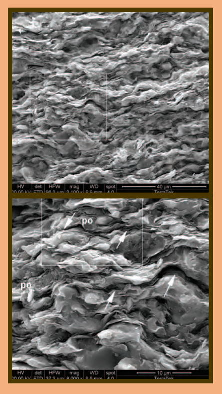

Medium magnification SEM view of phosphatic, argillaceous mudstone. Clay packets that make up the matrix are separated along parting surfaces, contributing to a fissile texture. The sample splits easily along closely spaced (<1 mm), brittle, wavy partings. The boxed area is enlarged in the image below.

SEM detail of part of the image above highlighting two flattened phosphatic/organic pods (po) with granular internal texture arranged along horizontal parting planes (arrows).

BSE IMAGES 5392.4 FT

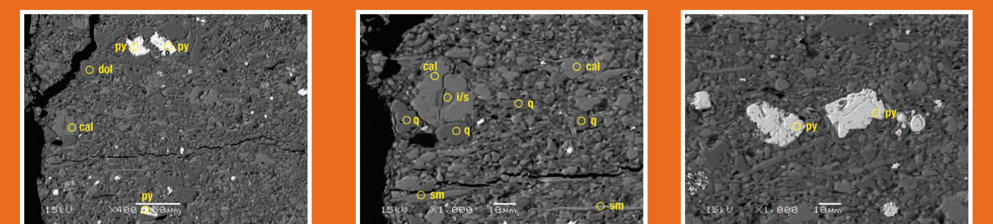

py = pyrite
dol = dolomite
cal = calcite
q = quatrz
sm = smectite
i/s = illite/ smectite

PANEL II

ANALYSIS OF NATURAL FRACTURES

Summary of hand sample descriptions of natural fractures in core: Natural fractures include: three inclined shear fractures or fracture zones and one horizontal shear fracture; fractures were slickensided and partially mineralized.

Annotation below images: Plane-polarized light thin section micrograph (PPL), crossed-polars thin section micrograph (XPL), Unstained thin section (no annotation), laser scanning confocal microscopy (LSCM), backscattered electron (BSE) image.

Depth: 5392.5 ft

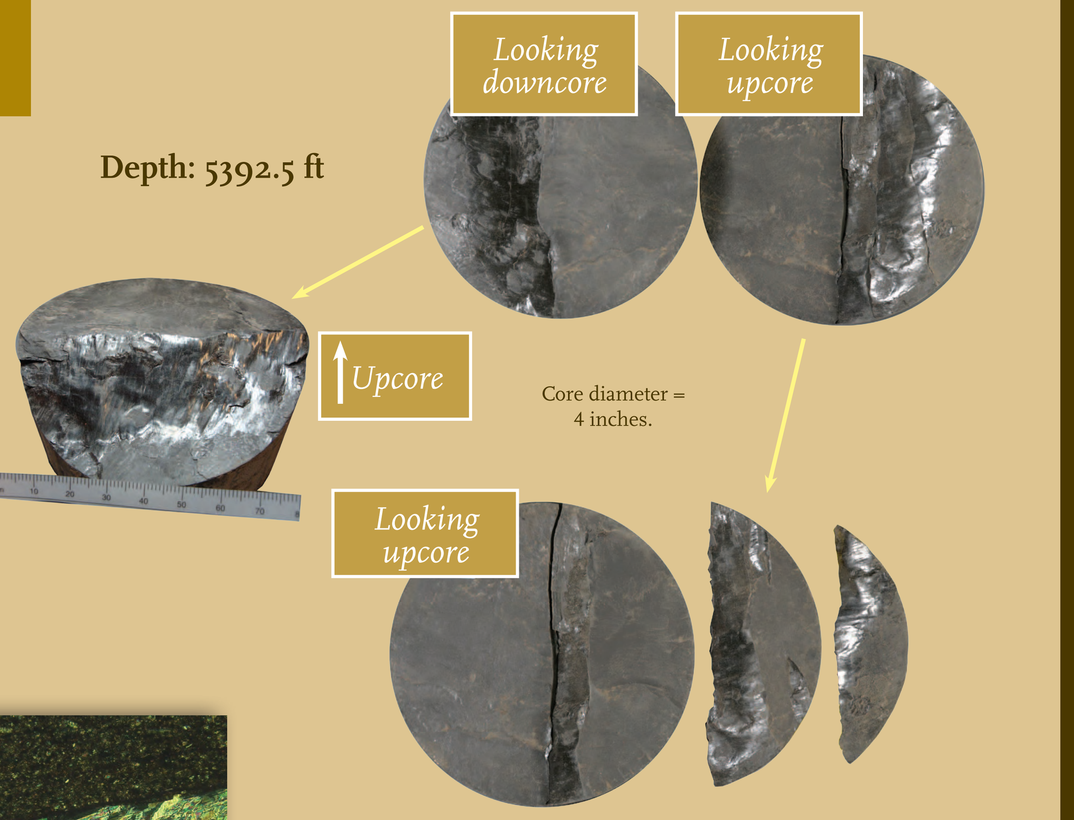

Core diameter = 4 inches.

Depth: 5392.5 ft to 5392.30 ft: Inclined shear fracture zone is undulous and contains multiple fracture surfaces; overall dip is 30°; thin sections and billets were cut perpendicular to the major inclined shear fracture.

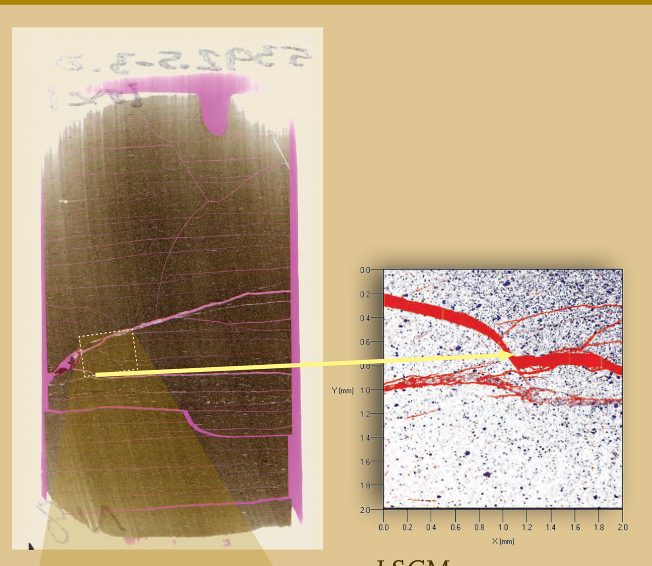

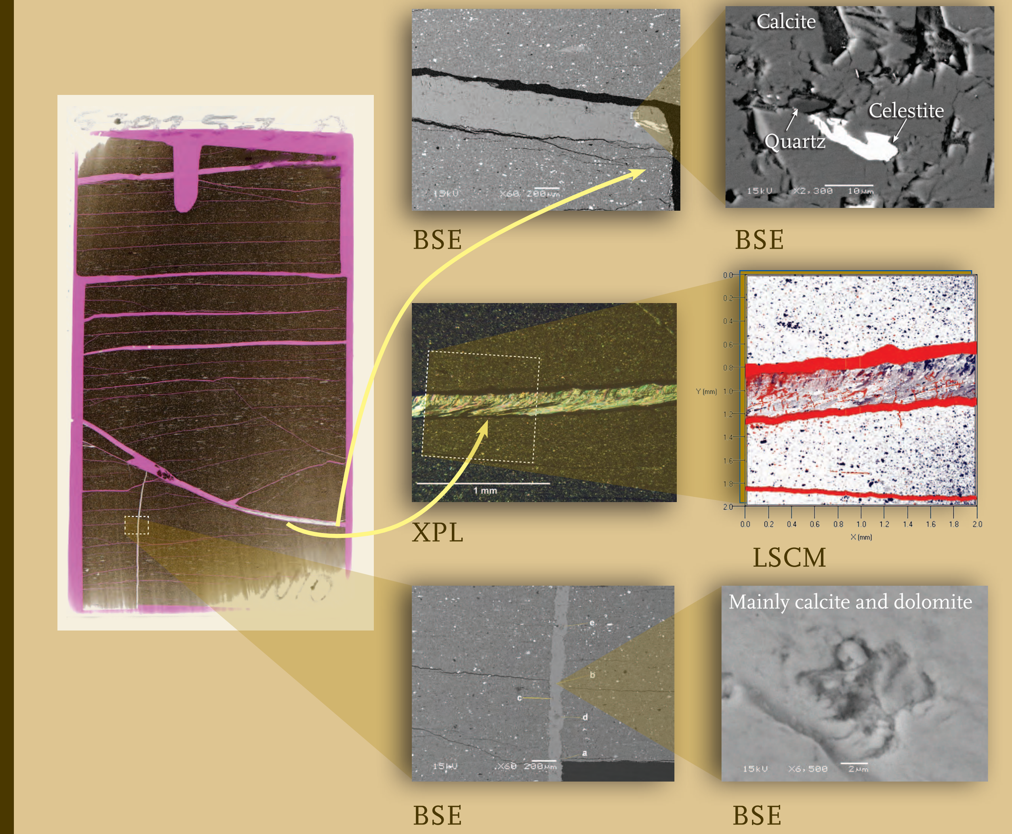

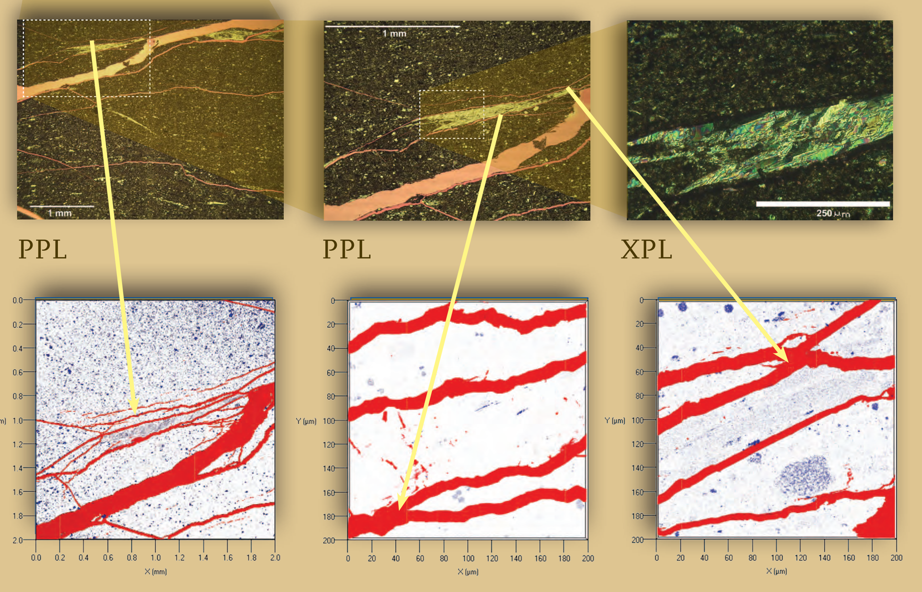

Methods

Connected porosity and organic material was imaged using a Zeiss 510-Meta Laser Scanning Confocal Microscope. 3D sections were measured at 5x (voxel size of 1.8 microns in x and y and 1.0 microns in z) using a Zeiss 5x/0.13NA HD DIC EC Epiplan-Neofluar lense and at 50 x (voxel size of 0.36 or 0.18 microns in x and y and 1.0 microns in z) using a Zeiss 50x/0.55NA DIC LD EC Epiplan-Neofluar lense. Porosity and organic material (including that associated with pyrite nodules) were simultaneously imaged using 543 nm excitation from a HeNe laser and a 560 nm long-pass filter for emissions from the rhodamine-dyed epoxy occupying connected pore spaces, and 477 nm excitation from an Ar laser and a 745-525 nm band-pass filter for emissions from organic material.

Thin sections and LSCM images reveal both extension and shear fractures. Dilational jogs and crack-seal textures are visible in the images. Fluorescent organics are co-located with precipitation in fractures. Preliminary microprobe analysis indicates that carbonates and sulfates dominate fracture mineralization. Fracture set orientations indicate maximum principal compressive stress is oriented vertically. The sense of shear is dextral.

Depth: 5392.6 ft: Horizontal shear fracture; thin sections and billets were cut perpendicular to the fracture.

Core diameter = 4 inches.
Depth might be incorrectly labeled on core.

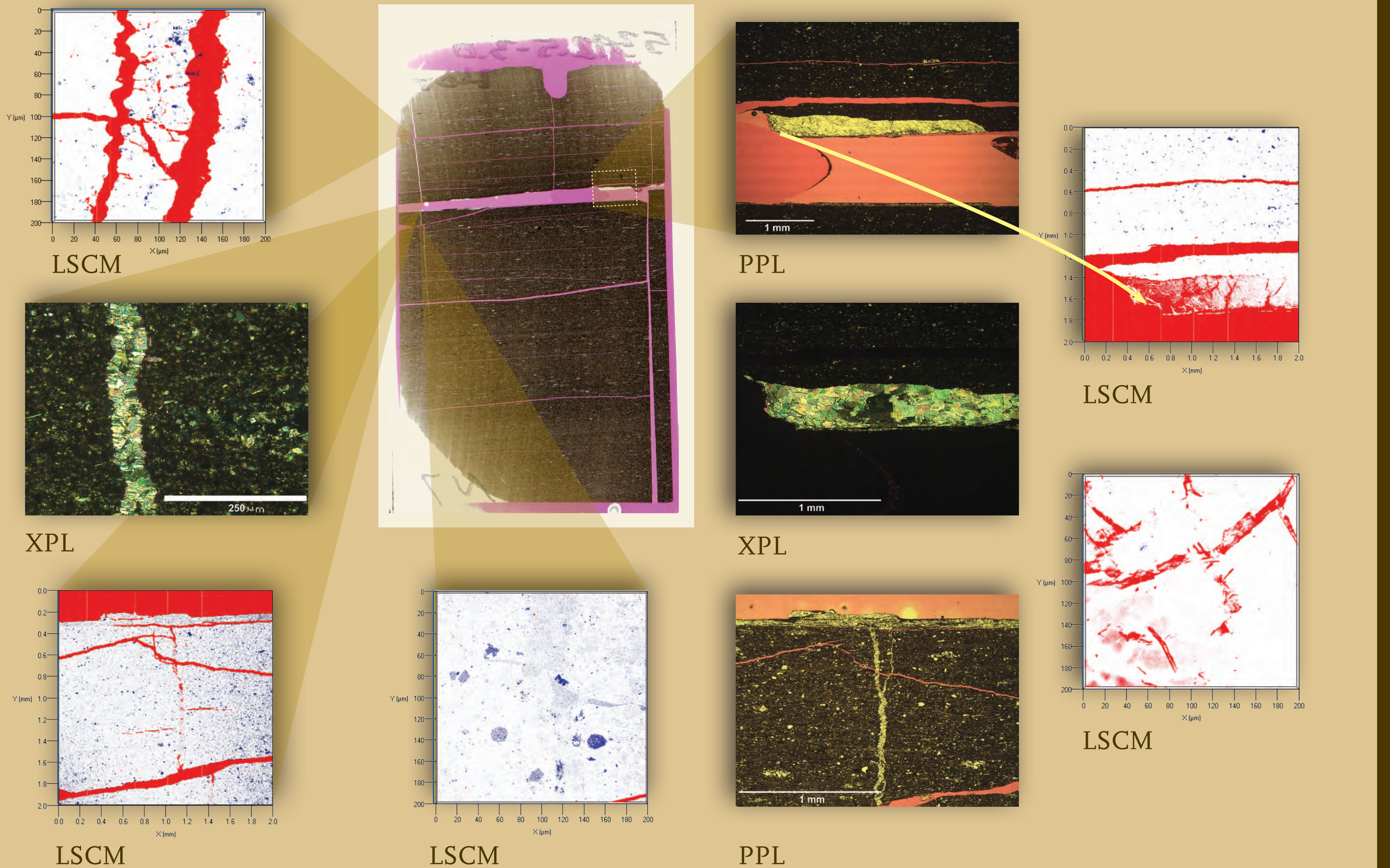

Fracture mineralization contains micro-porosity and does not show strong crystal orientation. Vertical fractures are extensional (see the LSCM image above with a fossil that is cut by a vertical fracture showing no shear displacement). Cross-cutting relationships could not be discerned; perhaps the precipitation occurred synchronously in the two types of fractures.

Petrophysical Properties

Summary of Petrophysical Reservoir Measurements

Depth (ft)	As-Received Bulk Density (g/cc)	As-Received Grain Density (g/cc)	Dry Grain Density (g/cc)	Porosity (% of BV)	Water Saturation (% of PV)	Gas Saturation (% of PV)	Mobile Oil Saturation (% of PV)	Gas-Filled Porosity (% of BV)	Bound Hydrocarbon Saturation (% of BV)	Bound Clay Water (% of BV)	Pressure-Decay Permeability (mD)
5379.40	2.570	2.623	2.648	3.35	19.55	60.61	19.84	2.03	1.14	6.56	0.000146
5382.80	2.561	2.597	2.621	2.72	24.73	50.88	24.39	1.38	1.33	7.01	0.000133
5386.90	2.572	2.615	2.649	3.51	30.07	47.71	22.22	1.67	0.90	7.42	0.000138
5390.80	2.522	2.573	2.614	4.30	36.18	46.05	17.77	1.98	1.47	7.46	0.000141

BV = bulk volume; PV = pore volume

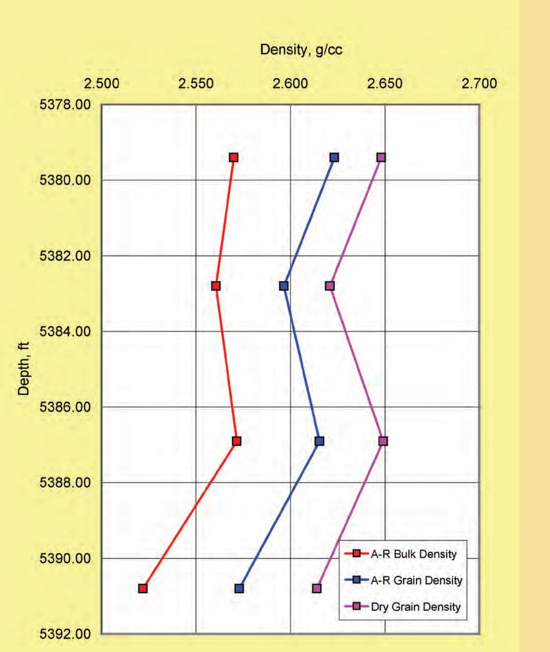

Density versus depth.

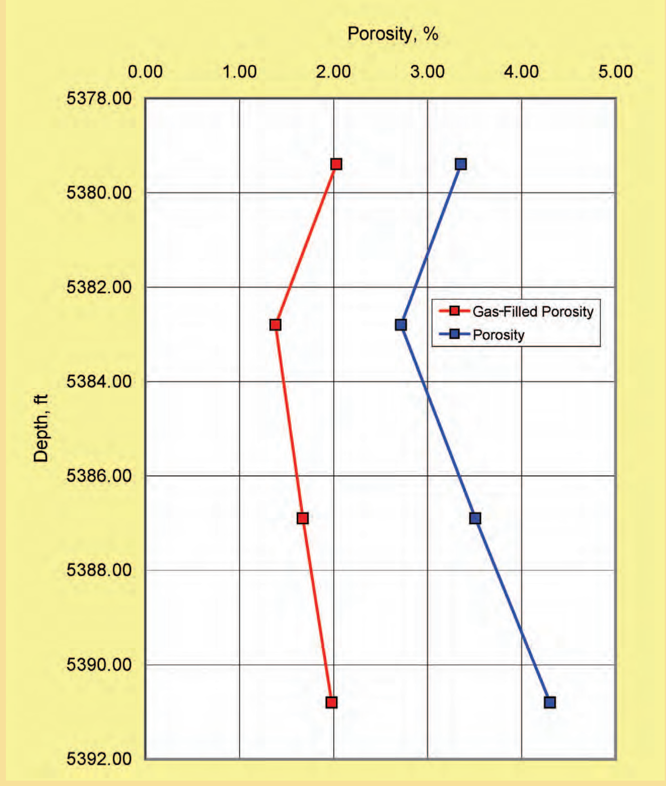

Porosity versus depth.

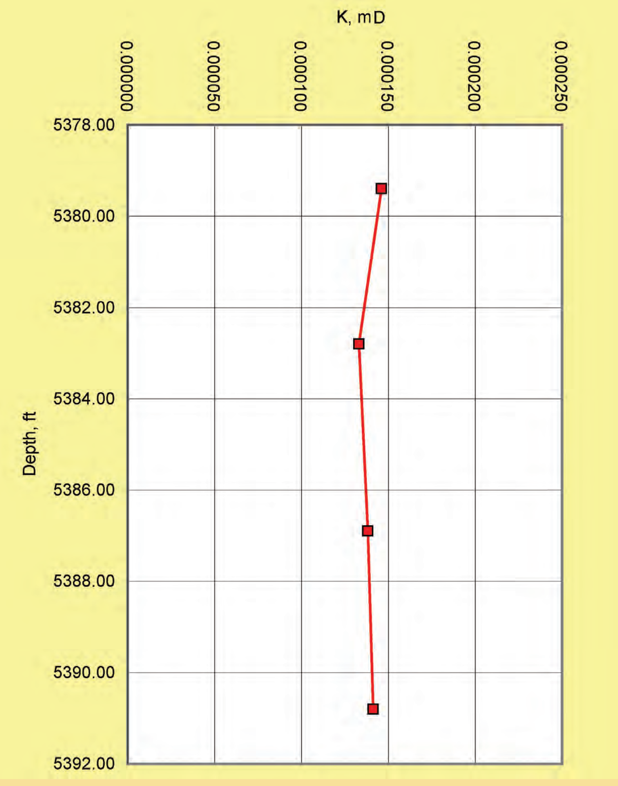

Permeability versus depth.

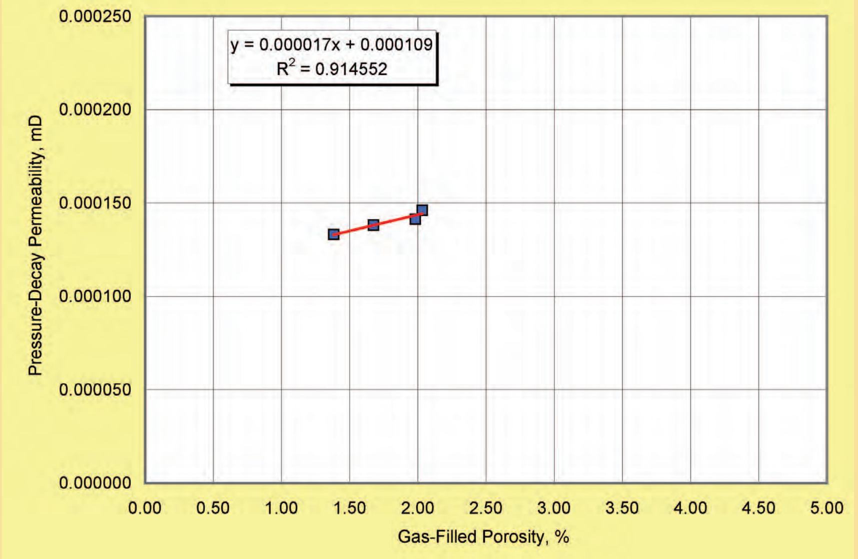

Gas-filled porosity versus pressure decay permeability.

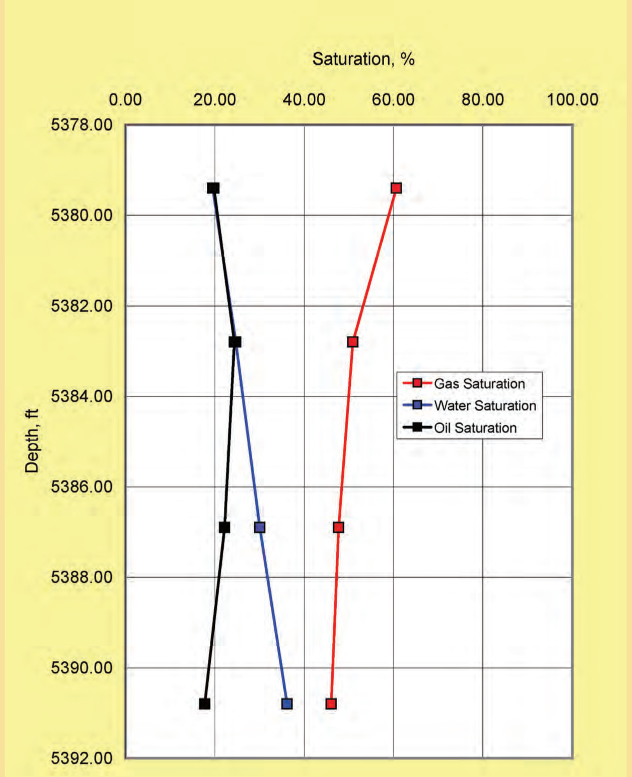

Saturation versus depth.

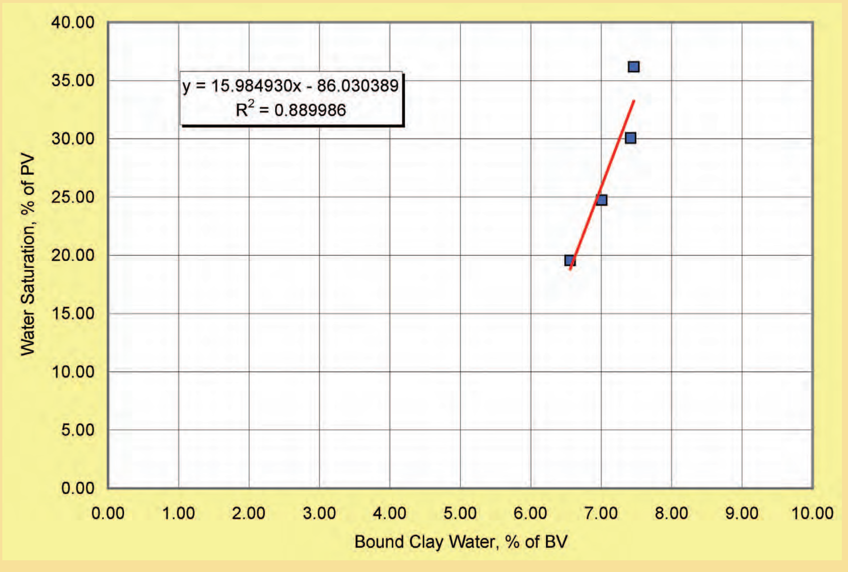

Bound clay water versus water saturation.

Mercury Injection Capillary Pressure and Pore Aperture Distributions

Vertical and horizontal plugs were jacketed with epoxy for directional mercury capillary pressure measurements on a Micromeritics AutoPore IV apparatus. The data is used to characterize pore aperture distributions and to predict the height of CO_2 and hydrocarbon columns that can be retained by the seal. The Gothic shale has very high seal capacity. The sample (the outlier) with the highest seal capacity was from the depth of 5378 ft.

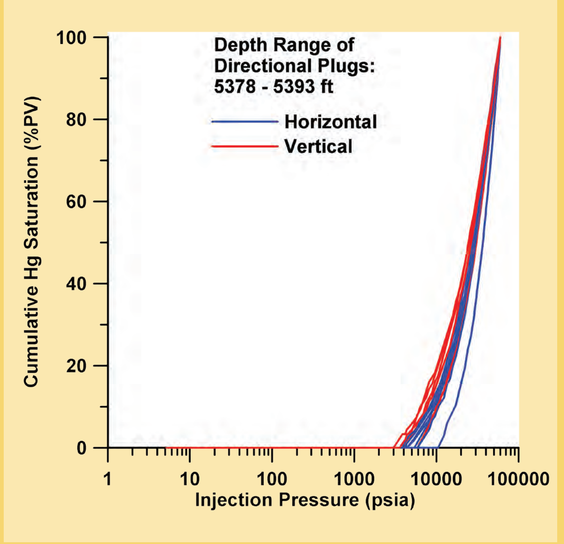

Cumulative mercury saturation versus injection pressure.

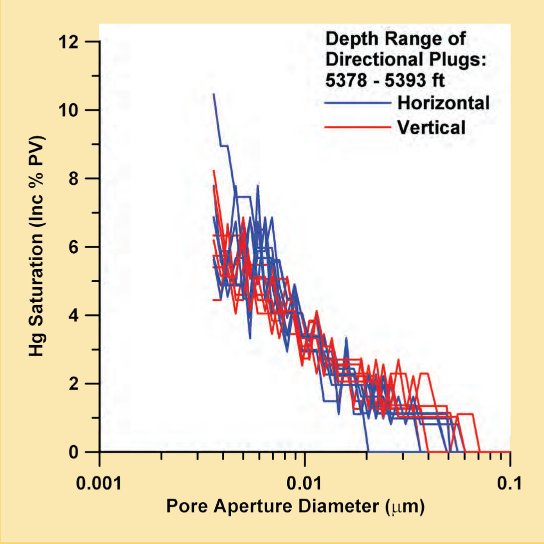

Mercury saturation versus pore aperture diameter.

Equations for Converting Mercury Injection Capillary Pressure Data to CO_2 Column Heights

$$P_c = \frac{4\sigma\cos\theta}{d} \qquad P_{b/CO_2} = P_{a/m}\frac{(\sigma_{b/CO_2}\cos\theta_{b/CO_2})}{(\sigma_{a/m}\cos\theta_{a/m})} \qquad h_{CO_2} = \frac{P_{th}}{(\rho_b - \rho_{CO_2})g}$$

P_c = capillary pressure
d = pore throat diameter
σ = interfacial tension
θ = contact angle for the CO_2/brine/rock system

P_{b/CO_2} or $P_{a/m}$ = capillary pressure in the brine/CO_2 or air/mercury system
σ_{b/CO_2} or $\sigma_{a/m}$ = interfacial tension of the brine/CO_2 or air/mercury system

P_{th} = threshold pressure, which is the pressure at which the non-wetting phase is assumed to form a continuous filament across the sample and can be determined from mercury capillary pressure measurements

ρ_b or ρ_{CO_2} = density of brine or CO_2
g = gravitational acceleration
h_{CO_2} = CO_2 column height

Geomechanics

Young's Modulus: 5381.18 - 5398.85 ft

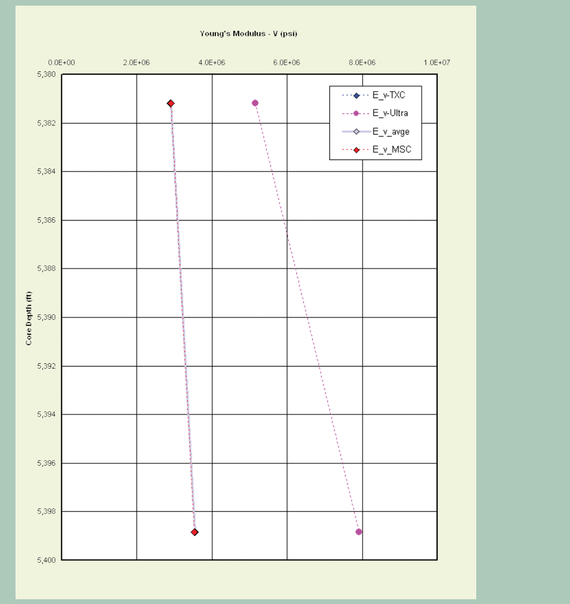

Vertical Young's modulus as a function of core depth. Averaged values are represented by the solid gray line.

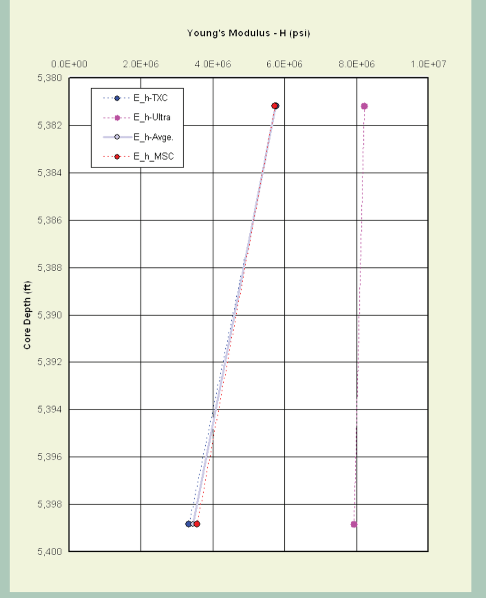

Horizontal Young's modulus as a function of core depth. Averaged values are represented by the solid gray line.

Poisson's Ratio: 5381.18 - 5398.85 ft

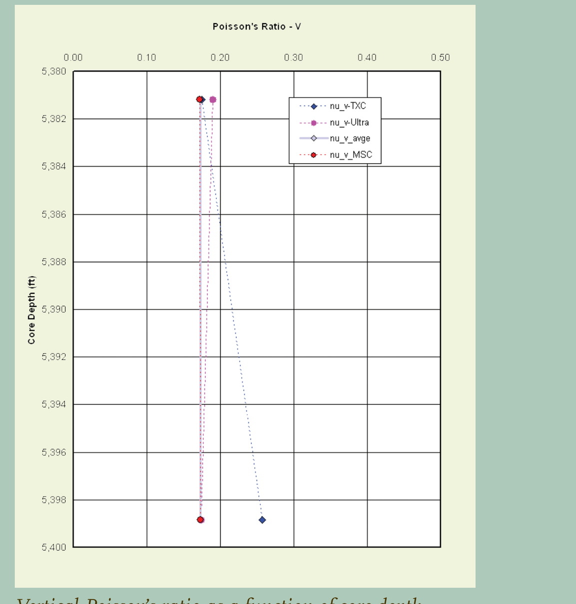

Vertical Poisson's ratio as a function of core depth. Averaged values are shown by the solid gray line.

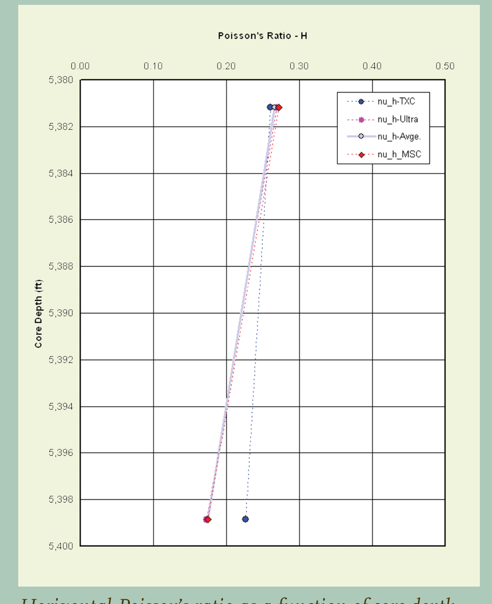

Horizontal Poisson's ratio as a function of core depth. Averaged values are shown by the solid gray line.

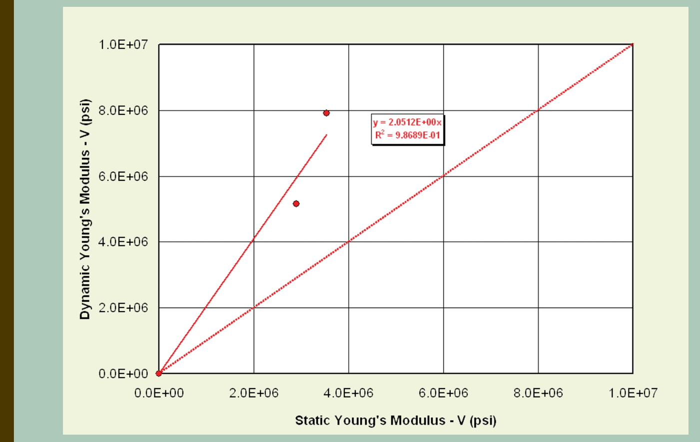

Vertical dynamic Young's modulus as a function of vertical static Young's modulus.

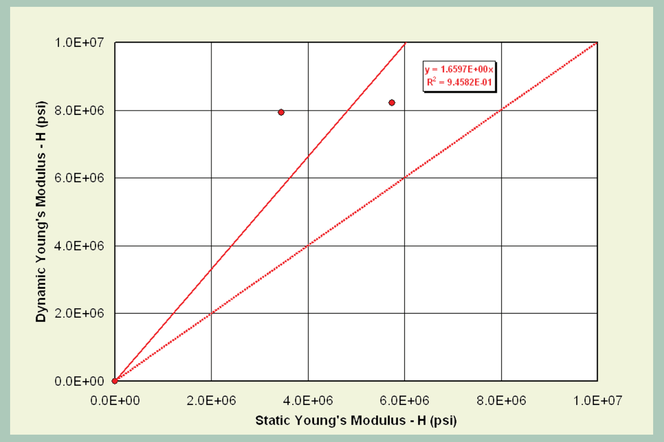

Horizontal dynamic Young's modulus as a function of horizontal static Young's modulus.

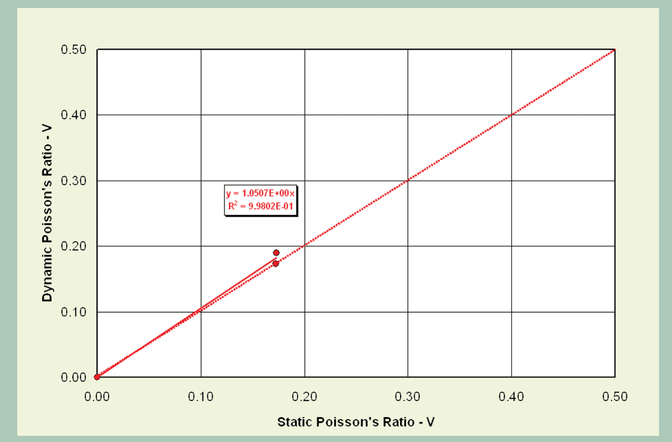

Vertical dynamic Poisson's ratio as a function of vertical static Poisson's ratio.

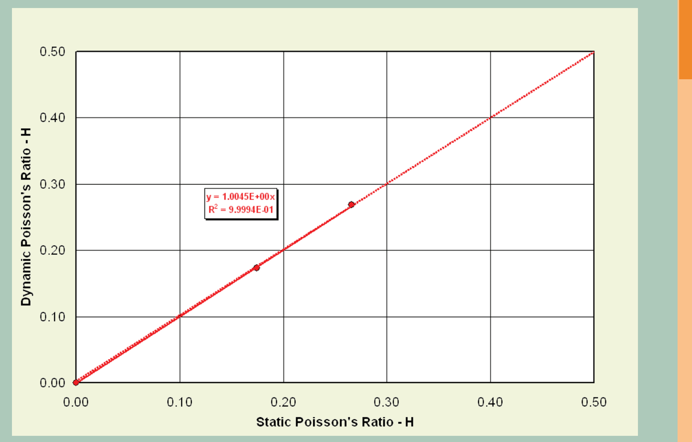

Horizontal dynamic Poisson's ratio as a function of horizontal static Poisson's ratio.

Summary of Multistress Anisotropy Measurements

Depth (ft)	Orientation	AR Bulk Density (g/cm^3)	Effective Mean Stress (psi)	Young's Modulus - Transverse (psi)	Young's Modulus - Axial (psi)	Poisson's Ratio - Transverse	Poisson's Ratio - Axial	Shear Modulus-Transverse (psi)
5381.20	Vertical	2.568	1994	2.897E+06	5.680E+06	0.186	0.274	1.156E+06
5381.20	45°	2.569	1994	2.926E+06	5.648E+06	0.167	0.268	1.164E+06
5381.15	Horizontal	2.574	1994	2.913E+06	5.849E+06	0.161	0.273	1.126E+06
5398.80	Vertical	2.283	1994	3.516E+06	3.601E+06	0.191	0.191	1.503E+06
5399.00	45°	2.316	1994	3.466E+06	3.638E+06	0.179	0.181	1.458E+06
5398.75	Horizontal	2.258	2004	3.597E+06	3.475E+06	0.148	0.150	1.470E+06

Notes: Transverse—Perpendicular to Bedding Plane. Axial—Parallel to bedding plane.

Compressional Testing: 5381.2-5398.8 ft

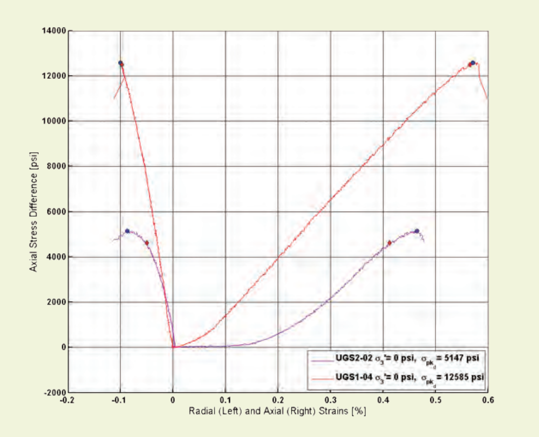

Axial stress difference versus radial and axial strains, measured during unconfined compression testing. The figure describes the evolution of rock deformation (i.e., axial and radial strains) and failure (i.e., yield stress, peak stress and residual strength - when available) during unconfined compression loading.

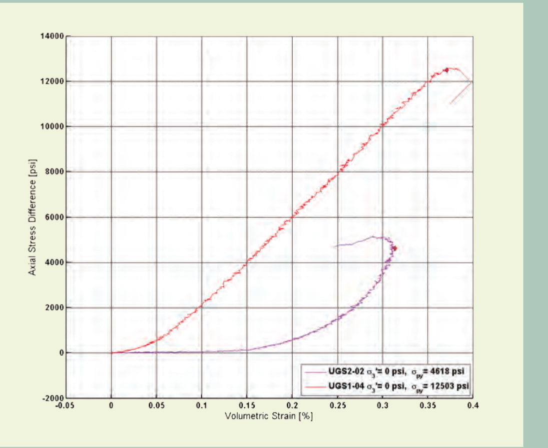

Axial stress difference versus volumetric strain, measured during unconfined compression testing. The figure describes the evolution of the rock deformation (dilation versus compaction) and the yield stress during unconfined compression loading.

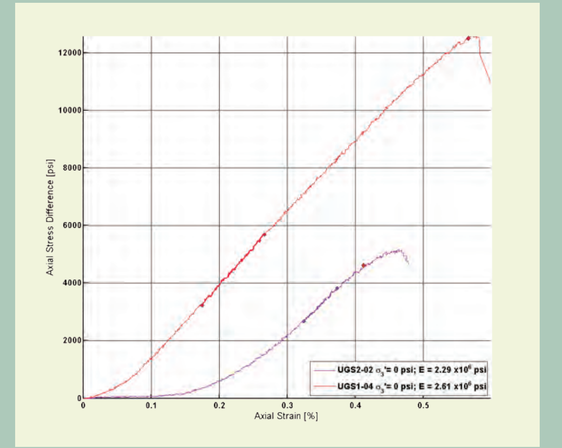

Axial stress difference versus axial strain, measured during unconfined compression testing. The figure describes the evolution of the axial modulus (Young's modulus) during unconfined compression loading.

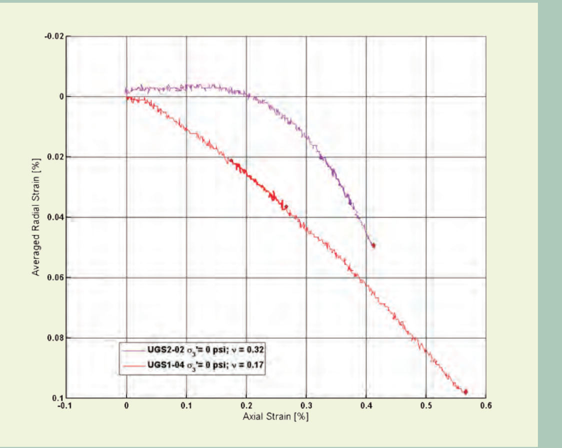

Averaged radial strain versus axial strain, measured during unconfined compression testing. The figure describes the evolution of the transverse modulus (Poisson's ratio) during unconfined compression loading.

Panel III

Continuous Unconfined Compressive Strength Profile

Scale = 0.1 ft

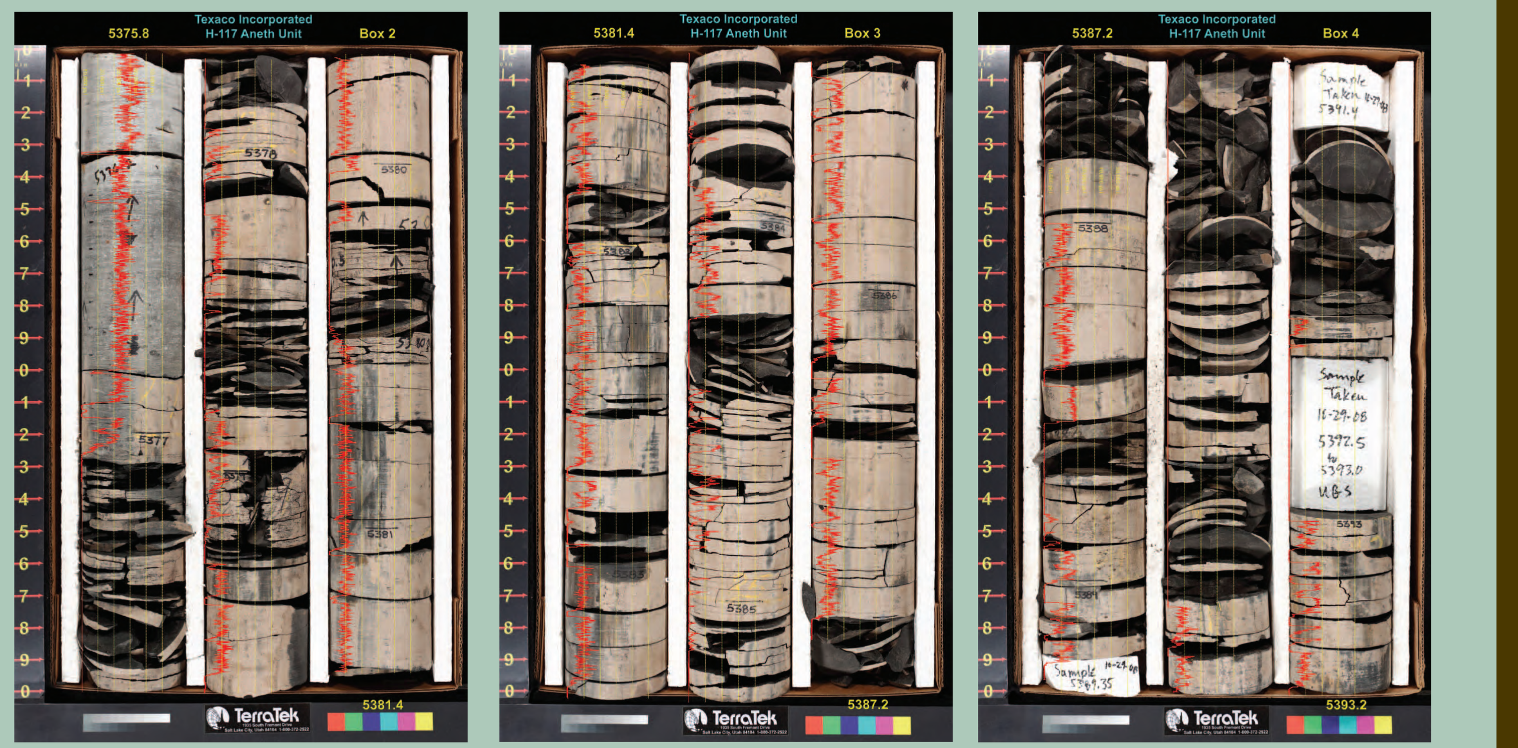

Conclusions

- The Gothic shale is an effective seal above the Desert Creek reservoir zone within the Pennsylvanian Paradox Formation, Aneth Unit, Greater Aneth field, San Juan County, Utah.
- The core from the Aneth Unit H-117 well is an excellent representation of the Gothic shale. The Gothic is remarkably uniform mudstone/shale with grain size ranging between mud and silt. Accessories and biological constituents consists of ubiquitous authigenic pyrite, microfossils, shell fragments, conodonts, and conularoids.
- Total organic carbon ranges from 2.2 to 4.4% with type II kerogen.
- Lithology consists of argillaceous or calcareous shale and mudstone composed of a clay to siliceous matrix with weak laminations defined by micas. Within the matrix calcite crystals, pyrite, quartz, microfossils, flakes of organics, and swarms of intercrystalline micropores are common.
- Porosity ranges from 2.7 to 3.4% and pressure-decay permeability is no greater than 0.000146 mD. These and other basic matrix petrophysical parameters indicate the Gothic shale to be a highly effective reservoir seal.
- The Gothic shale should support very large CO_2 or hydrocarbon columns based on mercury injection capillary pressure and pore aperture distributions analysis.
- Continuous unconfined compressive strength profiles show a relatively uniform homogenous shale package.
- Compressional testing suggests some degree of hydraulic fracture containment.
- Near the base of the Gothic section vertical to subvertical extensional fractures are present. Mineralization co-located with these natural fractures is most likely dominated by carbonates and organics.

Geomechanical data will be used to understand the nature of the fractures at the base of the Gothic and why they are not present higher in the section.

What are the impacts of organics on geochemical reactions with carbonates and CO_2-rich fluids?

Continued research by the Southwest Partnership will address these issues.

References

Amateis, L.J., 1995, Application of sequence stratigraphic modeling to integrated reservoir management at Aneth Unit, Greater Aneth field, Utah: Society of Petroleum Engineers, SPE Paper 030534, p. 35-49.

Harr, C.L., 1996, Paradox oil and gas potential of the Ute Mountain Ute Indian Reservation, *in* Huffman, A.C., Jr., Lund, W.R., and Godwin, L.H., editors, Geology of the Paradox Basin: Utah Geological Association Publication 25, p. 13-28.

Hite, R.J., 1960, Stratigraphy of the saline facies of the Paradox Member of the Hermosa Formation of southeastern Utah and southwestern Colorado, *in* Smith, K.G., editor, Geology of the Paradox Basin fold and fault belt: Four Corners Geological Society, Third Field Conference Guidebook, p. 86-89.

Hite, R.J., and Cater, F.W., 1972, Pennsylvanian rocks and salt anticlines, Paradox Basin, Utah and Colorado, *in* Mallory, W.W., editor, Geologic atlas of the Rocky Mountain region: Rocky Mountain Association of Geologists Guidebook, p. 133-138.

Kitcho, C.H., 1981, Characteristics of surface faults in the Paradox Basin, *in* Wiegnand, D.L., editor, Geology of the Paradox Basin: Rocky Mountain Association of Geologists Guidebook, p. 1-21.

Peterson, J.A., 1992, Aneth field – U.S.A., Paradox Basin, Utah, *in* Foster, N.H., and Beaumont, E.A., editors, Stratigraphic traps III: American Association of Petroleum Geologists Treatise of Petroleum Geology – Atlas of Oil and Gas Fields, p. 41-82.

Peterson, J.A., and Ohlen, H.R., 1963, Pennsylvanian shelf carbonates, Paradox Basin, *in* Bass, R.O., editor, Shelf carbonates of the Paradox basin: Four Corners, Geological Society Symposium, 4th Field Conference, p. 65-79.

Reid, F.S., and Berghorn, C.E., 1981, Facies recognition and hydrocarbon potential of the Pennsylvanian Paradox Formation, *in* Wiegand, D.L., editor, Geology of the Paradox Basin: Rocky Mountain Association of Geologists Guidebook, p. 111-117.

Dislcaimer

E&M_2009_02_C